



Rapid grain growth in post-AGB disc systems from far-infrared and sub-millimetre photometry

P. Scicluna ¹★, F. Kemper ^{1,2}, A. Trejo,¹ J. P. Marshall,¹ S. Ertel³ and M. Hillen⁴

¹Academia Sinica, Institute of Astronomy and Astrophysics, 11F Astronomy-Mathematics Building, NTU/AS Campus, No. 1, Section 4, Roosevelt Rd., Taipei 10617, Taiwan

²European Southern Observatory, Karl-Schwarzschild-Str. 2, D-85748 Garching b. München, Germany

³Steward Observatory, Department of Astronomy, University of Arizona, 993 N. Cherry Ave, Tucson, AZ 85721, USA

⁴Instituut voor Sterrenkunde, KU Leuven, Celestijnenlaan 200B, B-3001 Leuven, Belgium

Accepted 2020 January 30. Received 2020 January 29; in original form 2019 January 18

ABSTRACT

The time-scales on which astronomical dust grows remain poorly understood, with important consequences for our understanding of processes like circumstellar disc evolution and planet formation. A number of post-asymptotic giant branch (AGB) stars are found to host optically thick, dust- and gas-rich circumstellar discs in Keplerian orbits. These discs exhibit evidence of dust evolution, similar to protoplanetary discs; however, since post-AGB discs have substantially shorter lifetimes than protoplanetary discs, they may provide new insights on the grain-growth process. We examine a sample of post-AGB stars with discs to determine the far-infrared and sub-millimetre spectral index by homogeneously fitting a sample of data from *Herschel*, the Submillimeter Array (SMA), and the literature. We find that grain growth to at least hundreds of micrometres is ubiquitous in these systems, and that the distribution of spectral indices is more similar to that of protoplanetary discs than debris discs. No correlation is found with the mid-infrared colours of the discs, implying that grain growth occurs independently of the disc structure in post-AGB discs. We infer that grain growth to \sim millimetre sizes must occur on time-scales $<< 10^5$ yr, perhaps by orders of magnitude, as the lifetimes of these discs are expected to be $\lesssim 10^5$ yr and all objects have converged to the same state. This growth time-scale is short compared to the results of models for protoplanetary discs including fragmentation and may provide new constraints on the physics of grain growth.

Key words: stars: AGB and post-AGB – circumstellar matter – dust, extinction.

1 INTRODUCTION

Understanding grain growth in a variety of environments remains an important outstanding challenge in understanding interstellar dust. Grains are inferred to evolve in a variety environments, such as the Interstellar medium (ISM), molecular clouds, circumstellar environments, and AGN tori (e.g. Ossenkopf 1993; Juhász et al. 2010; Hirashita & Voshchinnikov 2014). These different environments correspond to very different regimes and mechanisms of dust processing, making them sensitive to different aspects of the physics. In planet formation, the growth of dust grains to millimetre sizes plays an important role, but the physics, primarily the time-scale, of growth to these sizes is an area of open debate. A wide variety of observations show evidence for grain growth at the later stages of planet formation (e.g. Ricci et al. 2010), and the current generation of models tends to successfully explain observations of grain growth in more evolved young stellar objects (YSOs) (e.g.

Birnstiel, Dullemond & Brauer 2010; Birnstiel & Andrews 2014). Some observations of the earlier stages of planet formation have also suggested grain growth, in some cases in tension with the models (e.g. Miotello et al. 2014). However, these are not the only astrophysical objects where large grains are observed, suggesting that complementary studies of other classes of objects may provide new insights on the process; if grains grow on similar or shorter time-scales under other comparable conditions, this would provide new constraints on the physics.

The final stage of the evolution of single low- and intermediate mass stars ($M \sim 1\text{--}8 M_{\odot}$) is heralded by the ejection of their envelope as they evolve off the asymptotic giant branch (AGB), exposing the core of the star as a white dwarf, ionizing the ejecta and producing a spectacular planetary nebula (PN). In particular, this phase is characterized by the development of strong asymmetries in the circumstellar medium. Many AGB envelopes are broadly spherical in shape, whereas a large fraction of PNe and pre-PNe host jets, tori, rings, or bipolar structures (e.g. Sahai et al. 2007). These asymmetries are, therefore, believed to develop either in the final phase of AGB evolution or in the initial post-AGB phase.

* E-mail: peter.scicluna@eso.org

In many cases, post-AGB stars are found to have a spectral energy distribution (SED) with a stronger near-infrared excess than would be expected for an expanding spherical shell; by analogy with protoplanetary discs (PPDs), it is assumed that these are host to a massive, dusty circumstellar disc that keeps dust in the hot, inner regions of the system (e.g. Van Winckel 2003; de Ruyter et al. 2005, 2006; Hillen et al. 2014; Gezer et al. 2015; Kamath, Wood & Van Winckel 2014, 2015). For a small number of sources, the disc nature has been confirmed by scattered light imaging (Osterbart, Langer & Weigelt 1997; Cohen et al. 2004; Ertel et al. 2019) or by observing gas in Keplerian rotation in the sub-millimetre (e.g. Bujarrabal et al. 2005, 2015, 2017, and further work by the same authors). Many of these systems have been found to be binaries, suggesting that the presence of a companion may play a role in the formation of the disc (Van Winckel et al. 2006; Oomen et al. 2018).

As stated above, other types of circumstellar discs, such as PPDs and debris discs (DDs) (e.g. Williams & Cieza 2011; Matthews et al. 2014; Wyatt et al. 2015), are typically populated by dust grains at least up to millimetre sizes, as probed by the spectral index in the far-infrared (FIR) and (sub-)millimetre wavelength ranges (e.g. Roccatagliata et al. 2009; Gáspár et al. 2012; MacGregor et al. 2016; Marshall et al. 2017). In PPDs, the existence of these large dust grains is believed to be linked to grain-growth processes, which can take place in such dense, long-lived (typical lifetimes are several megayears, e.g. Fedele et al. 2010) discs. There is also evidence for the presence of grains of such sizes in the discs in post-AGBs (Molster et al. 1999) in spite of the large difference in lifetime compared to PPDs (a factor of ~ 100 , compare, e.g. Fedele et al. 2010; Bujarrabal et al. 2017). It has also been noted that the SEDs of post-AGB discs have similar characteristics to PPDs (particularly Type II Herbig Ae/Be stars; de Ruyter et al. 2006) and that radiative-transfer models developed for PPDs also fit post-AGBs very effectively (Hillen et al. 2014, 2015), suggesting that the two environments may experience similar processes. However, to date such studies have either been relatively small (e.g. de Ruyter et al. 2005) or the samples used have combined both post-AGBs with discs with pre-PNe and other objects (e.g. Sahai et al. 2011), making it difficult to evaluate the prevalence of grain growth. Since post-AGB discs are expected to have very short lifetimes, if large grains are common, it could have significant consequences for our understanding of grain growth in circumstellar discs, placing strong constraints on the time-scale of this process.

In this paper, we present a systematic analysis of the FIR and sub-millimetre emission of post-AGB stars with discs and the relationship to grain growth in these objects. We exploit archival *Herschel*/SPIRE photometry along with new SMA observations and literature fluxes of a sample of 45 post-AGBs with discs to derive the spectral index and hence infer whether significant grain growth may have occurred. Based on this, we explore how the unique environments of these systems can constrain the physics of dust growth and the implications for the initial conditions of planet formation. In Section 2, we describe the observational data employed, and Section 3 outlines the methods used to analyse the data. In Section 4, we discuss the implications of our results. Finally, in Section 5, we summarize our findings.

2 OBSERVATIONS

2.1 Sample selection

Our sample is selected from the sample of RV Tauris with IR excess and confirmed binary post-AGBs of de Ruyter et al. (2006). We

select all sources in that sample that were observed with *Herschel*. In addition, we add the famous post-AGB binary the Red Rectangle, which has very deep ALMA photometry from Bujarrabal et al. (2013) and was also included in the de Ruyter et al. (2006) sample, although no *Herschel* data are available.

2.2 *Herschel*

We used data from the *Herschel Space Observatory's* (Pilbratt et al. 2010) FIR and sub-millimetre instruments Photodetector Array Camera and Spectrograph (PACS; Poglitsch et al. 2010) (70/100/160 μm) and Spectral and Photometric Imaging REceiver (SPIRE Griffin et al. 2010) (250/350/500 μm). Imaging observations of the targets were obtained from the *Herschel* Science Archive¹ as either level 2.5 (mosaic, pipeline-reduced) or level 3 (user-reduced) data products. In our analysis, we included data from the following observing programmes: KPOT_smolinar.1 (HiGAL – the *Herschel* Infrared Galactic Plane Survey; Molinari et al. 2010, 2016), OT2_smolinar_7, and OT2_cgiielen_4.

Herschel data analysis was carried out in the *Herschel* Interactive Processing Environment (HIPE; Ott 2010). The data were taken as science-ready products from the archive as described above. For the PACS wavebands, we used the JScanamorphos image, as it is the most reliable for retaining complex background structure through the spatial filtering that occurs in the map-making process. For aperture photometry, we adopted an aperture radius of 20 arcsec and a sky annulus of 30–40 arcsec. Measured fluxes in each band were adjusted with the appropriate aperture correction factors from Balog et al. (2014). For the SPIRE wavebands, we used the implementation of the sexttractor tool provided in HIPE to measure the fluxes. This is due to the bright and structured nature of the backgrounds at sub-millimetre wavelengths making aperture photometry inadvisable. The beam area and full-width half-maxima for each band were taken from the SPIRE observer's manual.² No colour corrections were applied to the fluxes. No frequency dependence was applied for the SPIRE maps (assumed ν^{-1} dependence, Rayleigh–Jeans tail is ν^2). A calibration uncertainty of 5 per cent is assumed for both PACS and SPIRE measurements.

2.3 Sub-millimetre array

Four of the science targets (RV Tau, AY Lep, PS Gem, and AR Pup) were observed on a single night (or track) on 2017 January 3, with eight antennae in compact configuration, giving baselines up to 77 m in length. The SMA can employ two receivers at the same time to effectively double the bandwidth available. The track used this observing mode, with both receivers tuned to an LO frequency of 225 GHz (1.3 mm), with 6 GHz continuum bandwidth per receiver per sideband. However, technical problems resulted in the loss of all data for baselines involving one antenna for one spectral chunk (2 GHz wide; channel width ~ 560 kHz). The remainder of the baselines for the affected chunk could still be used. Therefore, the fraction of data lost did not have a big impact in the final achieved sensitivity. Depending on elevation constraints, and some data lost during the calibration process, the final time on source was from ~ 1.5 to 2 h, per target. For the calibration, the SMA observed 3C 273 for bandpass, Uranus and 2232 + 117 for flux, and five more quasars for temporal amplitude and phase gains, interleaved in a loop with the science targets.

¹<http://archives.esac.esa.int/hsa/whsa/>

²http://herschel.esac.esa.int/Docs/SPIRE/html/spire_om.html

The data were calibrated using MIR,³ following the standard procedures. The imaging was done with the AIPS (Wells 1985) task IMAGR. The final rms varies across the continuum maps and is between 0.5 and ~ 1 mJy beam⁻¹. Only AR Pup and RV Tau were detected as unresolved continuum sources, with signal-to-noise ratios (SNR) of ~ 50 and 16, respectively.

The spectral setup was chosen to place the CO(2–1) line in the upper sideband. However, no line emission was detected towards any of the targets, even with re-binning up to ~ 7 km s⁻¹ and rms values down to ~ 20 mJy.

2.4 Literature

To improve sampling at longer wavelengths, we searched the literature for published sub-millimetre observations of the *Herschel*-observed sample. These fluxes are primarily taken from observations with SCUBA but also include observations from ALMA and at 1.3 and 3 mm from other facilities. A full list of fluxes is given in Table 1 along with the *Herschel* and SMA observations described above.

3 RESULTS

The observing data described in the previous section were used to derive spectral indices in the FIR-sub-millimetre region for all sources with detections in two or more bands at wavelengths of 250 μ m or longer. To ensure that the results of the fitting are robust, and can directly integrate the existence of upper limits on the fluxes in some filters, we employ the affine-invariant Markov-Chain Monte Carlo (MCMC) implementation EMCEE (Foreman-Mackey et al. 2013). Standard non-linear least-square minimizers are typically not able to handle censored data, e.g. upper or lower limits. However, in many cases, upper limits (left-censored data) on the flux provide important constraints on the spectral index, particularly for constraining non-detections at long wavelengths, and hence more advanced methods that are able to account for this are required. The treatment of upper limits is trivial in MCMC, allowing us to treat sources with different numbers of detections uniformly. The model being fitted is a straightforward power law, which becomes a straight line when fitted to the logarithm of the fluxes, i.e.

$$\log F_v = \alpha \log \lambda + b \quad (1)$$

where F_v is the flux density in milli-Jansky, λ is the observing wavelength, and α is the spectral index. As the colour corrections for the filters in question are typically at most a few per cent, we opt to work with this simple model as is rather than performing synthetic photometry. For a datum with $F_v/\sigma_{F_v} > 3$, our likelihood function is the familiar

$$\log \mathcal{L}_i = -\frac{1}{2} \frac{(\log F_{v,\text{obs}} - \log F_{v,\text{mod}})^2}{\delta_{F_v}^2} + \log(2\pi\delta_{F_v}^2) \quad (2)$$

where $F_{v,\text{obs}}$ and $F_{v,\text{mod}}$ are the observed and model fluxes, respectively, and δ_{F_v} is the fractional uncertainty σ_{F_v}/F_v , which corresponds to the uncertainty on $\log F_v$. For upper limits, this must be modified to correctly capture how well the limit constrains the model. In these cases, it is necessary to integrate the pdf of the upper limit, i.e.

$$\log \mathcal{L}_i = \log \int_0^{3\sigma_{F_v}} \mathcal{N}(F_{v,\text{mod}}, \sigma_{F_v}) dF_v \quad (3)$$

where $\mathcal{N}(F_{v,\text{mod}}, \sigma_{F_v})$ is a normal distribution with mean $F_{v,\text{mod}}$ and standard deviation σ_{F_v} . In this case, models that do not violate or approach the upper limit have broadly similar likelihoods at that wavelength, while models that do are strongly penalized. The final log-likelihood of a given model is then

$$\log \mathcal{L} = \sum \log \mathcal{L}_i \quad (4)$$

which is used as our objective function in the MCMC. This model naturally results in a tight anticorrelation between the slope and intercept of the line, but this is significant only for the sources with the most uncertain data.

To explore the influence of the choice of wavelength coverage, the fitting was repeated for different subsets of the data. The results of these fits are summarized in Table 2. Upon examining the results, it is clear that the inclusion of PACS fluxes biases the results towards shallower slopes. This is most likely a result of temperature effects – PACS samples wavelengths too close to the peak of the emission, and hence there is significant curvature in this region of the SED. As a result, we take the results for fits including all wavelengths ≥ 250 μ m (labelled ‘No PACS’ in Table 2) as our preferred set and use these in all further analyses. Using these fits, we predict fluxes at longer wavelengths in Table 3.

Using the full set of MCMC realizations (after an appropriate burn-in period), we construct an estimate of the distribution of spectral indices (see Fig. 1). The sharp peak at -2 results from the group of sources with long-wavelength data and very well constrained spectral indices, and the broader bump describes the wider population, with long tails towards very steep and very shallow slopes. A second peak exists at ~ -2.3 ; however it is unclear whether this reflects a genuine separation into two groups.

4 DISCUSSION

The data set shows a clear abundance of flat emission across the FIR-sub-millimetre range. The distributions of α are clearly dominated by values close to 2, regardless of the choice of data set. However, there are clear differences that depend on the choice of wavelengths used to derive α .

4.1 Importance of long-wavelength photometry

The choice of wavelength range over which to fit the spectral index has a significant effect on the outcome of the fit. Fig. 2 shows the fitted value of α as a function of the longest wavelength included in the fit. There is a clear reduction in the uncertainty on the spectral index as longer wavelengths are used. This is in part due to the increased number of points and partly a result of the larger separation in wavelength between the longest and shortest wavelengths. However, there is no real trend in the value of the spectral index.

The importance of the choice of wavelengths can also be explored by looking at the values of α derived for the same object with different wavelengths. In particular, the second and fourth columns of Table 2 can be compared for those objects with additional data. In general, the addition of longer wavelength data tends to result in a steeper slope by up to roughly 25 per cent. However, this trend results in a significant change⁴ only in the two cases of 89 Her and AC Her, which have a plethora of high-precision detections. There is one exception, TW Cam, where the slope becomes shallower,

³<https://www.cfa.harvard.edu/sma/smaMIR/>

⁴Defined as $\frac{|\Delta\alpha|}{\sqrt{\sigma_{\alpha_1} + \sigma_{\alpha_2}}} \geq 1$.

Table 1. Complete list of fluxes, in mJy, for our sample. Telescopes or instruments for the observations and their origin are noted in the references. Where not otherwise noted, fluxes are from *Herschel*.

Source	IRAS PSC	100	160	250	350	450	500	850	1300	3000
TW Cam	04166+5719	–	–	145 ± 10	74 ± 8	–	0 ± 7	11 ± 2.3 ^a	–	–
DY Ori	06034+1354	1431 ± 72	571 ± 32	223 ± 14	114 ± 9	–	0 ± 7	–	–	–
CT Ori	06072+0953	–	–	50 ± 8	0 ± 79	–	0 ± 56	–	–	–
SU Gem	06108+2743	819 ± 41	358 ± 22	166 ± 9	8 ± 6	–	0 ± 32	7.5 ± 2.5 ^a	–	–
UY CMa	06160–1701	162 ± 11	87 ± 23	22.5 ± 6.7	–	–	–	2.4 ± 2.1 ^a	–	–
V382 Aur	06338+5333	029 ± 5	49 ± 8	0 ± 7	–	–	–	–	–	–
ST Pup	06472–3713	362 ± 18	78 ± 9	30 ± 8	0 ± 13	–	–	–	–	–
V421 CMa	07140–2321	201 ± 11	29 ± 9	31 ± 8	0 ± 7	–	–	–	–	–
U Mon	07284–0940	9120 ± 456	4236 ± 212	2009 ± 104	1066 ± 54	–	549 ± 32	181.6 ± 2.6 ^a	100 ± 14 ^b	15 ± 0.3 ^b
V390 Vel	08544–4431	–	–	4229 ± 220	1863 ± 97	–	588 ± 34	–	–	–
BZ Pyx	09060–2807	242 ± 13	126 ± 11	0 ± 9	–	–	–	–	–	–
IRAS 09144–4933	09144–4933	1107 ± 55	379 ± 31	0 ± 14	–	–	–	–	–	–
IRAS 09400–4733	09400–4733	582 ± 29	270 ± 17	112 ± 7	45 ± 5	–	0 ± 7	–	–	–
GP Cha	09538–7622	163 ± 9	56 ± 9	0 ± 10	–	–	–	–	–	–
AG Ant	10158–2844	479 ± 24	235 ± 13	72 ± 8	54 ± 7	–	53 ± 9	8.7 ± 2.8 ^c	–	–
HR 4226	10456–5712	–	–	2158 ± 111	1093 ± 58	–	530 ± 30	–	–	–
V802 Car	11000–6153	1545 ± 77	983 ± 163	0 ± 14	–	–	–	–	–	–
GK Car	11118–5726	169 ± 11	109 ± 14	0 ± 36	–	–	–	–	–	–
AF Crt	11472–0800	321 ± 17	80 ± 10	29 ± 8	24 ± 8	–	0 ± 7	–	–	–
RU Cen	12067–4508	–	–	589 ± 31	319 ± 18	–	149 ± 12	–	–	–
SX Cen	12185–4856	–	–	83 ± 9	45 ± 8	–	0 ± 7	–	–	–
V1123 Cen	12222–4652	2446 ± 122	928 ± 46	292 ± 17	126 ± 10	–	49 ± 80	–	–	–
IRAS 13258–8103	13258–8103	660 ± 33	458 ± 31	143 ± 8	51 ± 80	–	0 ± 7	–	–	–
EN Tra	14524–6838	1459 ± 73	625 ± 33	266 ± 16	139 ± 10	–	75 ± 11	–	–	–
IRAS 15469–5311	15469–5311	3880 ± 194	1441 ± 75	0 ± 49	–	–	–	–	–	–
IRAS 15556–5444	15556–5444	2987 ± 149	1363 ± 72	660 ± 35	319 ± 18	–	169 ± 0.13	–	–	–
NSV 7708	16230–3410	254 ± 13	75 ± 8	41 ± 80	0 ± 11	–	–	–	–	–
IRAS 17038–4815	17038–4815	1878 ± 94	994 ± 55	447 ± 25	268 ± 16	–	105 ± 11	–	–	–
LR Sco	17243–4348	762 ± 38	334 ± 29	86 ± 8	45 ± 6	–	60 ± 8	–	–	–
89 Her	17534+2603	–	–	667 ± 36	343 ± 20	–	160 ± 13	40.9 ± 2.4 ^c	9.2 ± 0.5 ^d	2.7 ± 0.3 ^d
AI Sco	17530–3348	1424 ± 71	631 ± 32	301 ± 17	14 ± 9	–	68 ± 8	–	–	–
V2053 Oph	18123+0511	1213 ± 61	390 ± 22	107 ± 10	32 ± 7	–	0 ± 7	–	–	–
IRAS 18158–3445	18158–3445	375 ± 19	135 ± 11	1328 ± 66	655 ± 33	–	314 ± 16	–	–	–
AC Her	18281+2149	–	–	1572 ± 83	817 ± 44	–	380 ± 22	99.4 ± 3.8 ^a	38 ± 1 ^b	4.6 ± 0.4 ^b
AD Aql	18564–0814	156 ± 12	93 ± 8	35 ± 8	0 ± 7	–	–	–	–	–
EP Lyr	19163+2745	107 ± 7	80 ± 10	37 ± 8	26 ± 7	–	22 ± 7	–	–	–
BD-02 4931	19157–0247	823 ± 41	408 ± 22	151 ± 11	93 ± 9	–	41 ± 8	–	–	–
QY Sge	20056+1834	–	–	372 ± 22	191 ± 13	–	108 ± 14	218 ± 1.8 ^e	–	–
AR Pup	08011–3627	–	–	1610 ± 83	861 ± 96	–	429 ± 72	–	41.6 ± 2.1 ^f	–
RV Tau	04440+2605	2414 ± 121	987 ± 49	512 ± 28	263 ± 18	–	135 ± 16	50.3 ± 3.6 ^a	15 ± 0.8 ^f	3.9 ± 0.2 ^b
AY Lep	05208–2035	680 ± 34	244 ± 12	102 ± 12	31 ± 10	–	0 ± 7	–	0 ± 1 ^f	–
PS Gem	07008+1050	338 ± 17	143 ± 12	75 ± 16	63 ± 15	–	24 ± 7	2.8 ± 1.9 ^c	0 ± 1 ^f	–
IRAS 17233–4330	17233–4330	1024 ± 13	496 ± 30	278 ± 41	208 ± 48	–	132 ± 34	–	–	–
BD + 03 3950	19125+0343	2331 ± 11	893 ± 27	313 ± 22	136 ± 21	–	84 ± 19	–	–	–
IW Car	09256–6324	–	–	2687 ± 30	1415 ± 27	–	685 ± 26	200 ± 20 ^g	–	–
Red Rectangle	06176–1036	–	–	–	–	3400 ± 200 ^h	–	62.5 ± 3.5 ^h	–	–

^aSCUBA, de Ruyter et al. (2005). ^bCARMA, Sahai et al. (2011). ^cSCUBA, de Ruyter et al. (2006). ^dPdBI, Bujarrabal et al. (2007). ^eSCUBA, Gledhill et al. (2002). ^fSMA, this work. ^gALMA, Bujarrabal et al. (2017). ^hALMA, Bujarrabal et al. (2013).

Table 2. Spectral indices for different choices of data set.

Source	SPIRE only	<i>Herschel</i>	No <i>Herschel</i>	No PACS	All data
TW Cam	$-3.05 \pm_{-0.58}^{0.51}$	$-3.03 \pm_{-0.58}^{0.48}$	$-2.54 \pm_{-1.67}^{1.73}$	$-2.50 \pm_{-0.33}^{0.32}$	$-2.49 \pm_{-0.32}^{0.31}$
DY Ori	$-3.33 \pm_{-0.42}^{0.39}$	$-2.36 \pm_{-0.11}^{0.11}$	–	$-3.30 \pm_{-0.43}^{0.38}$	$-2.36 \pm_{-0.11}^{0.11}$
SU Gem	$-2.20 \pm_{-0.62}^{0.61}$	$-1.81 \pm_{-0.14}^{0.14}$	$-2.55 \pm_{-1.64}^{1.73}$	$-2.19 \pm_{-0.62}^{0.61}$	$-1.81 \pm_{-0.14}^{0.14}$
UY CMa	$-2.56 \pm_{-1.66}^{1.73}$	$-1.94 \pm_{-0.69}^{0.66}$	$-2.46 \pm_{-1.73}^{1.69}$	$-3.10 \pm_{-1.28}^{1.39}$	$-2.19 \pm_{-0.58}^{0.44}$
U Mon	$-1.88 \pm_{-0.25}^{0.25}$	$-1.74 \pm_{-0.10}^{0.09}$	$-1.98 \pm_{-0.04}^{0.05}$	$-1.98 \pm_{-0.04}^{0.03}$	$-1.93 \pm_{-0.03}^{0.03}$
V390 Vel	$-2.83 \pm_{-0.26}^{0.25}$	$-2.83 \pm_{-0.26}^{0.25}$	–	$-2.84 \pm_{-0.25}^{0.25}$	$-2.84 \pm_{-0.26}^{0.26}$
IRAS 09400-4733	$-3.12 \pm_{-0.60}^{0.62}$	$-2.03 \pm_{-0.14}^{0.13}$	–	$-3.11 \pm_{-0.71}^{0.62}$	$-2.03 \pm_{-0.14}^{0.14}$
AG Ant ^a	$-0.69 \pm_{-0.25}^{0.45}$	$-1.66 \pm_{-0.17}^{0.17}$	$-2.52 \pm_{-1.69}^{1.71}$	$-1.13 \pm_{-0.49}^{0.48}$	$-1.69 \pm_{-0.16}^{0.16}$
HR 4226	$-2.03 \pm_{-0.25}^{0.26}$	$-2.03 \pm_{-0.25}^{0.25}$	–	$-2.03 \pm_{-0.25}^{0.25}$	$-2.02 \pm_{-0.25}^{0.26}$
AF Crt	$-2.36 \pm_{-1.48}^{1.35}$	$-2.54 \pm_{-0.39}^{0.39}$	–	$-2.42 \pm_{-1.50}^{1.38}$	$-2.54 \pm_{-0.40}^{0.38}$
RU Cen	$-1.95 \pm_{-0.31}^{0.31}$	$-1.96 \pm_{-0.31}^{0.31}$	–	$-1.97 \pm_{-0.31}^{0.31}$	$-1.95 \pm_{-0.30}^{0.30}$
SX Cen	$-2.85 \pm_{-0.96}^{0.81}$	$-2.86 \pm_{-0.97}^{0.81}$	–	$-2.87 \pm_{-0.97}^{0.83}$	$-2.83 \pm_{-0.96}^{0.81}$
V1123 Cen	$-2.51 \pm_{-0.67}^{0.67}$	$-2.36 \pm_{-0.15}^{0.15}$	–	$-2.50 \pm_{-0.66}^{0.66}$	$-2.36 \pm_{-0.15}^{0.15}$
IRAS 13258-8103	$-3.91 \pm_{-0.74}^{0.86}$	$-2.02 \pm_{-0.13}^{0.12}$	–	$-3.91 \pm_{-0.73}^{0.86}$	$-2.02 \pm_{-0.13}^{0.13}$
EN TrA	$-1.87 \pm_{-0.45}^{0.44}$	$-1.87 \pm_{-0.13}^{0.13}$	–	$-1.86 \pm_{-0.45}^{0.45}$	$-1.87 \pm_{-0.13}^{0.13}$
IRAS 15556-5444	$-1.99 \pm_{-0.30}^{0.30}$	$-1.78 \pm_{-0.11}^{0.11}$	–	$-1.99 \pm_{-0.30}^{0.30}$	$-1.78 \pm_{-0.11}^{0.10}$
IRAS 17038-4815	$-1.95 \pm_{-0.49}^{0.38}$	$-1.66 \pm_{-0.11}^{0.11}$	–	$-1.94 \pm_{-0.36}^{0.37}$	$-1.65 \pm_{-0.12}^{0.12}$
LR Sco	$-0.71 \pm_{-0.49}^{0.42}$	$-1.95 \pm_{-0.16}^{0.16}$	–	$-0.72 \pm_{-0.49}^{0.43}$	$-1.95 \pm_{-0.15}^{0.16}$
89 Her	$-2.01 \pm_{-0.32}^{0.32}$	$-2.04 \pm_{-0.31}^{0.31}$	$-2.31 \pm_{-0.23}^{0.23}$	$-2.45 \pm_{-0.08}^{0.08}$	$-2.45 \pm_{-0.08}^{0.08}$
AI Sco	$-2.18 \pm_{-0.39}^{0.39}$	$-1.83 \pm_{-0.12}^{0.12}$	–	$-2.21 \pm_{-0.38}^{0.40}$	$-1.84 \pm_{-0.12}^{0.12}$
V2053 Oph	$-3.63 \pm_{-0.23}^{0.89}$	$-2.74 \pm_{-0.20}^{0.19}$	–	$-3.71 \pm_{-0.83}^{0.96}$	$-2.74 \pm_{-0.20}^{0.19}$
IRAS 18158-3445	$-2.08 \pm_{-0.26}^{0.23}$	$-0.03 \pm_{-0.04}^{0.02}$	–	$-2.08 \pm_{-0.23}^{0.24}$	$-0.03 \pm_{-0.04}^{0.02}$
AC Her	$-2.05 \pm_{-1.04}^{0.26}$	$-2.04 \pm_{-0.26}^{0.27}$	$-2.40 \pm_{-0.16}^{0.16}$	$-2.32 \pm_{-0.06}^{0.06}$	$-2.32 \pm_{-0.06}^{0.06}$
EP Lyr	$-1.22 \pm_{-0.59}^{0.80}$	$-1.02 \pm_{-0.30}^{0.29}$	–	$-1.23 \pm_{-1.04}^{0.81}$	$-1.03 \pm_{-0.29}^{0.30}$
BD-02 4931	$-1.70 \pm_{-0.59}^{0.58}$	$-1.81 \pm_{-0.15}^{0.15}$	–	$-1.71 \pm_{-0.58}^{0.59}$	$-1.80 \pm_{-0.15}^{0.15}$
QY Sge	$-1.85 \pm_{-0.41}^{0.43}$	$-1.85 \pm_{-0.43}^{0.42}$	$-2.48 \pm_{-1.71}^{1.70}$	$-2.28 \pm_{-0.19}^{0.18}$	$-2.29 \pm_{-0.19}^{0.19}$
AR Pup	$-1.89 \pm_{-0.50}^{0.50}$	$-1.90 \pm_{-0.50}^{0.50}$	$-2.53 \pm_{-1.67}^{1.73}$	$-2.23 \pm_{-0.10}^{0.10}$	$-2.22 \pm_{-0.10}^{0.10}$
RV Tau	$-1.94 \pm_{-0.39}^{0.39}$	$-1.75 \pm_{-0.12}^{0.12}$	$-1.90 \pm_{-0.15}^{0.14}$	$-2.00 \pm_{-0.06}^{0.06}$	$-1.92 \pm_{-0.04}^{0.04}$
AY Lep	$-3.64 \pm_{-0.89}^{0.99}$	$-2.30 \pm_{-0.21}^{0.19}$	$-2.55 \pm_{-1.68}^{1.72}$	$-3.70 \pm_{-0.84}^{0.91}$	$-2.35 \pm_{-0.20}^{0.17}$
PS Gem	$-1.67 \pm_{-1.11}^{0.98}$	$-1.60 \pm_{-0.25}^{0.25}$	$-2.55 \pm_{-1.67}^{1.69}$	$-2.75 \pm_{-0.74}^{0.55}$	$-1.91 \pm_{-0.16}^{0.13}$
IRAS 17233-4330	$-1.20 \pm_{-0.86}^{0.73}$	$-1.41 \pm_{-0.18}^{0.18}$	–	$-1.21 \pm_{-0.85}^{0.73}$	$-1.41 \pm_{-0.18}^{0.18}$
BD + 03 3950	$-2.07 \pm_{-0.68}^{0.66}$	$-2.12 \pm_{-0.10}^{0.10}$	–	$-2.08 \pm_{-0.66}^{0.67}$	$-2.12 \pm_{-0.10}^{0.10}$
IW Car	$-1.95 \pm_{-0.10}^{0.10}$	$-1.94 \pm_{-0.11}^{0.11}$	$-2.48 \pm_{-1.71}^{1.70}$	$-1.98 \pm_{-0.09}^{0.10}$	$-1.99 \pm_{-0.09}^{0.10}$
Red Rectangle	–	–	$-2.67 \pm_{-0.28}^{0.29}$	$-2.66 \pm_{-0.30}^{0.29}$	$-2.66 \pm_{-0.30}^{0.29}$

^aSPIRE wavelengths are contaminated with background emission.

possibly because of the lack of 500- μ m detection, which warrants further investigation.

A further important consideration is whether these changes in spectral index are real or an artefact of biases. This factor is considered below in Section 4.2, where we explore the role of confounding effects in detail.

4.2 Link between spectral index and grain growth

Although grain growth does cause shallow spectral indices, can we exclude other mechanisms that produce the same effect? These can broadly be divided into three cases:

- (i) different emission mechanisms, e.g. free–free emission;
- (ii) radiative-transfer effects arising from high optical depth or low dust temperatures; or
- (iii) changes in dust refractive indices.

The first of these can be easily examined through observations at centimetre wavelengths. Where this has been done (e.g. Sahai

et al. 2011), it has been shown that the free–free contribution at wavelengths ≤ 3 mm is negligible, and that the 0.3–3 mm emission is dominated by dust in post-AGB discs.

The role temperature and opacity effects can, to a certain extent, be seen in the change of α as different wavelength ranges are included in the fit. In particular, the inclusion of PACS observations, which lie close to the peak of the Planck function for the temperatures expected for an optically thick circumstellar disc, biases the fit towards shallower spectral indices. As explored above, this trend does not continue for longer wavelengths, with the inclusion of millimetre wavelengths primarily reducing the uncertainties on α rather than modifying the best-fitting value. While this can be conclusively excluded only by combining spatially resolved multiwavelength observations with detailed radiative-transfer modelling, the lack of any trend of the calculated α values with wavelength suggests that it does not impact the findings of our analysis in any significant manner.

The final case could arise from changes in dust composition, or perhaps from a dependence of the optical constants on dust

Table 3. Predicted sub-millimetre fluxes (mJy) for sources detected in two or more bands, based on MCMC samples.

Source	α	450	850	1.3 mm	3 mm
TW Cam	$-2.50 \pm_{-0.33}^{+0.32}$	$33 \pm_5^5$	$6.8 \pm_{-1.9}^{+2.5}$	$2.4 \pm_{-0.9}^{+1.3}$	$0.29 \pm_{-0.15}^{+0.29}$
DY Ori	$-3.30 \pm_{-0.43}^{+0.33}$	$36 \pm_6^7$	$4.4 \pm_{-1.6}^{+2.1}$	$1.1 \pm_{-0.5}^{+0.8}$	$0.068 \pm_{-0.04}^{+0.09}$
CT Ori	$-2.46 \pm_{-1.72}^{+1.66}$	$12 \pm_8^{+21}$	$2.4 \pm_{-2.2}^{+16.4}$	$0.9 \pm_{-0.8}^{+12.6}$	$0.1 \pm_{-0.1}^{+6.8}$
SU Gem	$-2.19 \pm_{-0.62}^{+0.61}$	$46 \pm_{-12}^{+16}$	$11 \pm_6^{+11}$	$4.5 \pm_{-2.8}^{+6.9}$	$0.72 \pm_{-0.56}^{+2.29}$
UY CMA	$-3.10 \pm_{-1.28}^{+1.39}$	$3.7 \pm_{-2.3}^{+5.0}$	$0.52 \pm_{-0.41}^{+2.20}$	$0.14 \pm_{-0.12}^{+1.15}$	$0.010 \pm_{-0.009}^{+0.291}$
ST Pup	$-2.82 \pm_{-1.50}^{+1.77}$	$5.5 \pm_{-3.5}^{+9.5}$	$0.9 \pm_{-0.8}^{+6.2}$	$0.27 \pm_{-0.25}^{+4.28}$	$0.026 \pm_{-0.025}^{+1.866}$
V421 CMA	$-3.14 \pm_{-1.32}^{+1.72}$	$4.5 \pm_{-2.6}^{+5.9}$	$0.59 \pm_{-0.47}^{+3.32}$	$0.16 \pm_{-0.14}^{+1.95}$	$0.011 \pm_{-0.011}^{+0.620}$
U Mon	$-1.98 \pm_{-0.25}^{+0.03}$	$640 \pm_{-25}^{+27}$	$182 \pm_5^5$	$79 \pm_2^2$	$15.1 \pm_{-0.6}^{+0.7}$
V390 Vel	$-2.84 \pm_{-0.25}^{+0.25}$	$833 \pm_{-78}^{+85}$	$137 \pm_{-29}^{+37}$	$41 \pm_{-12}^{+17}$	$3.8 \pm_{-1.6}^{+2.8}$
IRAS 09400-4733	$-3.11 \pm_{-0.71}^{+0.62}$	$18 \pm_6^7$	$2.6 \pm_{-1.4}^{+2.6}$	$0.68 \pm_{-0.45}^{+1.11}$	$0.051 \pm_{-0.041}^{+0.174}$
AG Ant	$-1.13 \pm_{-0.25}^{+0.48}$	$40 \pm_8^{+10}$	$20 \pm_7^{+12}$	$12 \pm_6^{+11}$	$4.7 \pm_{-3.1}^{+8.8}$
HR 4226	$-2.03 \pm_{-0.25}^{+0.25}$	$655 \pm_{-62}^{+68}$	$180 \pm_{-38}^{+49}$	$76 \pm_{-22}^{+31}$	$14 \pm_6^{+10}$
AF Crt	$-2.42 \pm_{-0.31}^{+1.38}$	$8.4 \pm_{-4.4}^{+7.6}$	$1.8 \pm_{-1.5}^{+5.7}$	$0.65 \pm_{-0.58}^{+4.02}$	$0.086 \pm_{-0.083}^{+1.865}$
RU Cen	$-1.97 \pm_{-0.97}^{+0.31}$	$188 \pm_{-23}^{+26}$	$54 \pm_{-14}^{+20}$	$23 \pm_8^{+13}$	$4.5 \pm_{-2.2}^{+4.5}$
SX Cen	$-2.87 \pm_{-0.83}^{+0.83}$	$17 \pm_6^8$	$2.7 \pm_{-1.8}^{+3.9}$	$0.80 \pm_{-0.62}^{+1.94}$	$0.073 \pm_{-0.066}^{+0.42}$
V1123 Cen	$-2.50 \pm_{-0.66}^{+0.66}$	$67 \pm_{-19}^{+26}$	$14 \pm_7^{+15}$	$4.7 \pm_{-3.0}^{+8.3}$	$0.59 \pm_{-0.46}^{+2.20}$
IRAS 13258-8103	$-3.91 \pm_{-0.73}^{+0.86}$	$14 \pm_5^9$	$1.2 \pm_{-0.7}^{+2.2}$	$0.23 \pm_{-0.16}^{+0.69}$	$0.086 \pm_{-0.072}^{+0.62}$
EN TrA	$-1.86 \pm_{-0.45}^{+0.45}$	$88 \pm_{-16}^{+20}$	$27 \pm_{-10}^{+17}$	$12 \pm_6^{+12}$	$2.6 \pm_{-1.7}^{+4.8}$
IRAS 15556-5444	$-1.99 \pm_{-0.30}^{+0.30}$	$201 \pm_{-24}^{+27}$	$57 \pm_{-15}^{+20}$	$24 \pm_8^{+13}$	$4.6 \pm_{-2.3}^{+4.5}$
IRAS 17038-4815	$-1.94 \pm_{-0.36}^{+0.37}$	$149 \pm_{-22}^{+25}$	$43 \pm_{-13}^{+19}$	$19 \pm_8^{+13}$	$3.7 \pm_{-2.1}^{+4.8}$
LR Sco	$-0.72 \pm_{-0.49}^{+0.43}$	$52 \pm_{-10}^{+12}$	$33 \pm_{-13}^{+18}$	$24 \pm_{-12}^{+21}$	$13 \pm_9^{+22}$
89 Her	$-2.45 \pm_{-0.08}^{+0.08}$	$171 \pm_{-11}^{+11}$	$36 \pm_2^2$	$13 \pm_1^1$	$1.6 \pm_{-0.2}^{+0.2}$
AI Sco	$-2.21 \pm_{-0.38}^{+0.40}$	$82 \pm_{-13}^{+16}$	$20 \pm_7^{+10}$	$7.9 \pm_{-3.4}^{+6.2}$	$1.2 \pm_{-0.7}^{+1.8}$
V2053 Oph	$-3.71 \pm_{-0.83}^{+0.96}$	$12 \pm_5^8$	$1.2 \pm_{-0.7}^{+2.3}$	$0.24 \pm_{-0.18}^{+0.85}$	$0.011 \pm_{-0.094}^{+0.098}$
IRAS 18158-3445	$-2.08 \pm_{-0.23}^{+0.24}$	$392 \pm_{-34}^{+36}$	$105 \pm_{-21}^{+26}$	$43 \pm_{-12}^{+16}$	$7.6 \pm_{-3.1}^{+5.1}$
AC Her	$-2.32 \pm_{-0.06}^{+0.06}$	$441 \pm_{-24}^{+25}$	$100 \pm_4^4$	$37 \pm_2^2$	$5.3 \pm_{-0.5}^{+0.5}$
AD Aql	$-3.14 \pm_{-1.29}^{+1.65}$	$4.9 \pm_{-2.7}^{+6.1}$	$0.65 \pm_{-0.50}^{+3.36}$	$0.17 \pm_{-0.15}^{+1.92}$	$0.012 \pm_{-0.012}^{+0.581}$
EP Lyr	$-1.23 \pm_{-1.04}^{+0.81}$	$19 \pm_7^7$	$8.8 \pm_{-5.7}^{+11.8}$	$5.2 \pm_{-4.0}^{+11.7}$	$1.9 \pm_{-1.7}^{+9.8}$
BD-02 4931	$-1.71 \pm_{-0.58}^{+0.59}$	$56 \pm_{-14}^{+18}$	$19 \pm_{-8.8}^{+17}$	$9.2 \pm_{-5.4}^{+13.0}$	$2.2 \pm_{-1.6}^{+6.5}$
QY Sge	$-2.28 \pm_{-0.19}^{+0.18}$	$102 \pm_{-9}^{+10}$	$24 \pm_{-3.7}^{+4.6}$	$9.0 \pm_{-1.9}^{+2.5}$	$1.3 \pm_{-0.4}^{+0.6}$
AR Pup	$-2.23 \pm_{-0.10}^{+0.10}$	$449 \pm_{-35}^{+37}$	$109 \pm_9^{+10}$	$42 \pm_5^5$	$6.6 \pm_{-1.1}^{+1.3}$
RV Tau	$-2.00 \pm_{-0.06}^{+0.06}$	$156 \pm_{-10}^{+11}$	$44 \pm_3^3$	$19 \pm_1^1$	$3.5 \pm_{-0.3}^{+0.4}$
AY Lep	$-3.70 \pm_{-0.84}^{+0.91}$	$12 \pm_5^8$	$1.1 \pm_{-0.7}^{+2.1}$	$0.23 \pm_{-0.17}^{+0.73}$	$0.010 \pm_{-0.009}^{+0.082}$
PS Gem	$-2.75 \pm_{-0.74}^{+0.55}$	$21 \pm_6^8$	$3.8 \pm_{-2.0}^{+2.5}$	$1.2 \pm_{-0.8}^{+1.2}$	$0.12 \pm_{-0.09}^{+0.25}$
IRAS 17233-4330	$-1.21 \pm_{-0.85}^{+0.73}$	$141 \pm_{-46}^{+62}$	$66 \pm_{-39}^{+76}$	$39 \pm_{-28}^{+76}$	$14 \pm_{-12}^{+63}$
BD + 03 3950	$-2.08 \pm_{-0.66}^{+0.67}$	$91 \pm_{-27}^{+39}$	$24 \pm_{-13}^{+28}$	$10 \pm_6^{+19}$	$1.8 \pm_{-1.4}^{+7.1}$
IW Car	$-1.98 \pm_{-0.09}^{+0.10}$	$841 \pm_{-39}^{+42}$	$238 \pm_{-24}^{+27}$	$102 \pm_{-14}^{+16}$	$19 \pm_4^5$
Red Rectangle	$-2.66 \pm_{-0.30}^{+0.29}$	$34 \pm_4^5$	$6.3 \pm_{-0.8}^{+0.9}$	$2.0 \pm_{-0.4}^{+0.5}$	$0.22 \pm_{-0.08}^{+0.13}$

temperature (e.g. Mennella et al. 1998; Boudet et al. 2005; Zeidler, Mutschke & Posch 2015). This is most difficult to exclude, as it may also introduce some wavelength dependence of the spectral index. However, these effects typically introduce a change in the spectral index by at most ± 1 . As the distribution of α values is very sharply constrained to the region $-2.5 \leq \alpha \leq -2$, it is clear that only a part of the difference from interstellar dust (expected to have $\alpha \sim -3.6$ based on Planck Collaboration XI 2014) could come from changes in composition or temperature-dependent opacity.

It is therefore clear that a significant fraction of the sources in our sample have undergone grain growth to sizes sufficient to alter the spectral index, although whether this is the only effect at play requires further observations. Models of the variation of FIR/(sub-)millimetre dust opacity with grain size suggest that, in order to

produce the values we observe, the grains must have grown to sizes at least ~ 1 mm (e.g. fig. 4 in Testi et al. 2014a) if grain growth alone is responsible. Even assuming that 50 per cent of the variation arises due to other effects (i.e. a change in α of ~ 0.5 – 0.8 needs to be explained), the dust in these discs must have grown to ~ 500 μ m (Testi et al. 2014a).

4.3 Mid-IR – far-IR comparison

de Ruyter et al. (2006) showed that post-AGB disc sources are most similar to the Type II Herbig Ae/Be stars, rather than Type I HAeBe or T Tauri stars. As the distinction between Type I and II is believed to be related to the structure of the discs (e.g. Garufi et al. 2017), we also explore the relationship between the mid-infrared

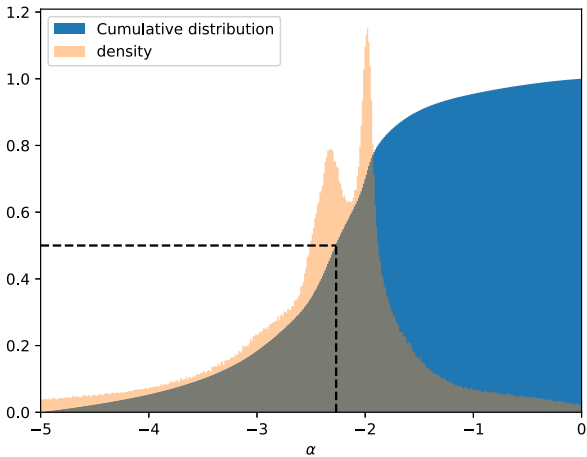


Figure 1. Histogram of the distribution of α values from MCMC realizations, produced by merging the full set of MCMC samples after burn in for all sources with detections in two or more bands, after removing AG Ant, AF Cr1, and EP Lyr, which have poor-quality fits. Including these sources would increase the tails of the distribution without affecting the core of the density. The dashed line indicates the median of the distribution.

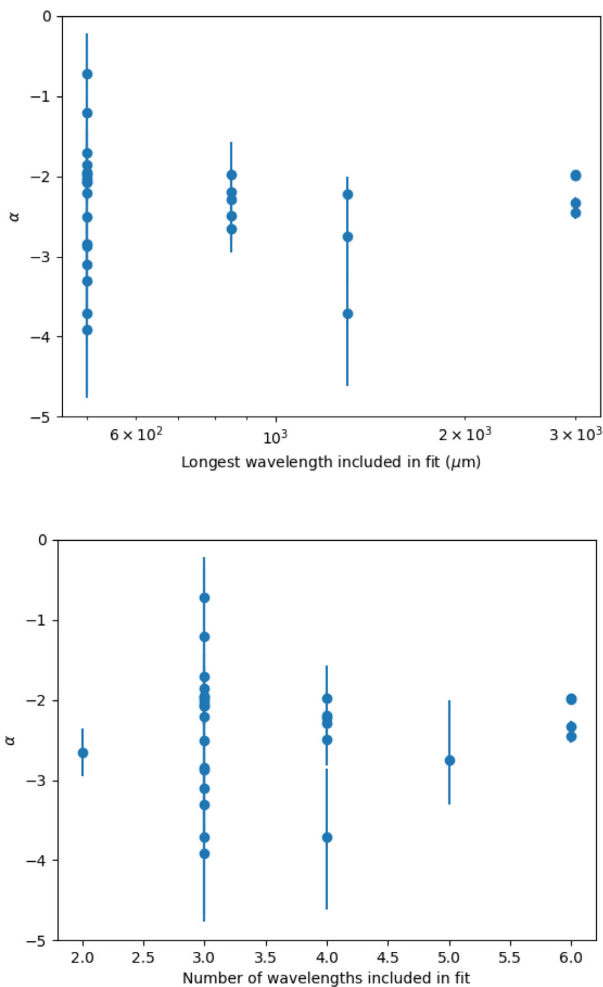


Figure 2. Fitted spectral index as a function of the longest wavelength included in the fit.

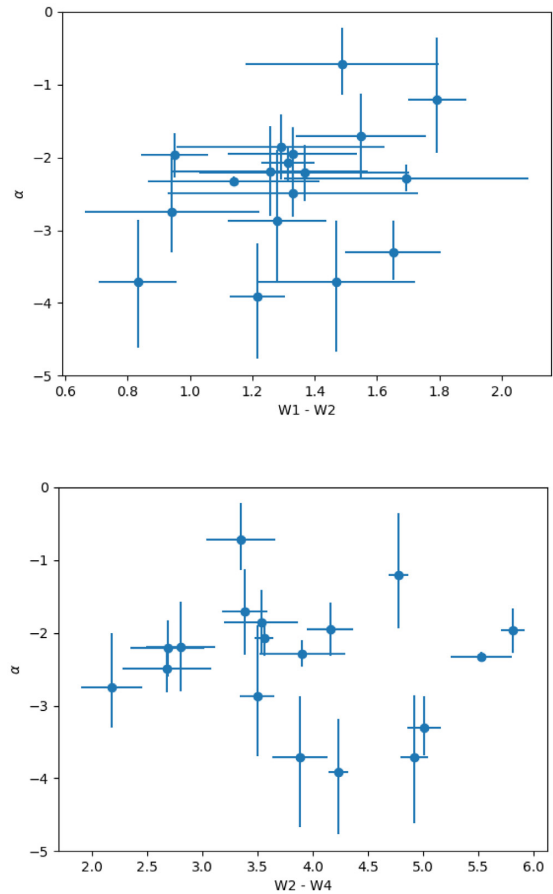


Figure 3. *Top:* *WISE* W1–W2 against α *Bottom:* W2–W4 against α . No correlations between these observables are apparent.

colours, which are expected to reflect the inner-disc structure, and the spectral index in Fig. 3. We obtain photometry of our targets at near- and mid-infrared wavelengths from the *Wide-field Infrared Survey Explorer's* AllWISE catalogue (Wright et al. 2010). *WISE* covered the whole sky in four wavebands (denoted W1 to W4, respectively) with effective wavelengths of 3.4, 4.6, 12, and 22 μm . The W1–W2 colour is sensitive to the hottest dust, and hence we expect it to probe how close the inner rim of the disc is to the sublimation radius: the redder the colour, the cooler the dust and hence the further it is from the sublimation radius. The W2–W4 colour, on the other hand, reflects the ratio of dust at ~ 800 K and at ~ 200 K; red colours indicate that the disc hosts a large gap or inner hole. However, neither plot shows a strong correlation with α . A weak correlation is visible with the W1–W2 colour, but it is possible that this is attributable to a change in the mid-infrared properties of the dust with grain growth (larger grains tend to be cooler) rather than a trend in which discs with larger inner radii have larger grains. No correlation is apparent between the W1–W2 colour and the orbital period of the binary (where available), indicating that disc–binary interaction does not dominate the location of the warmest dust/disc inner edge.

Another way of examining this comparison between grain growth and the mid-IR colours of the discs is to consider the fraction of stellar radiation reprocessed by the discs. Using the ratio of L_{IR}/L_{\star} calculated by de Ruyter et al. (2006), we look for a correlation in Fig. 4. As above, this does not reveal any evidence for a trend, with roughly uniform scatter. We expect that the precision of the alpha

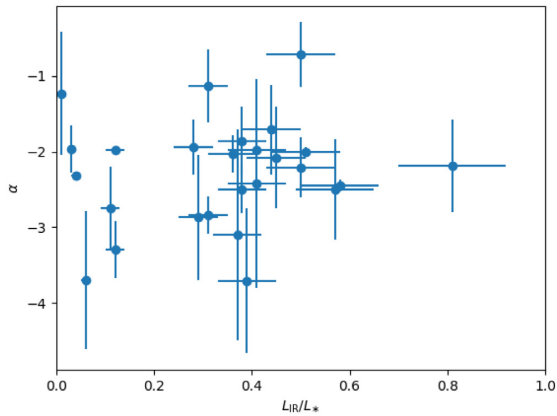


Figure 4. Scatter plot of the fraction of the stellar luminosity reprocessed in the infrared (data from de Ruyter et al. 2006) against α . No correlation is apparent, and significantly higher precision on α would be required to probe a relationship.

determination must reach the 1 percent level (an improvement in precision of roughly two orders of magnitude, corresponding to our most precise alpha measurements with the longest lever-arm in wavelength) before it is useful to explore this relationship, or a factor of 10 more sources must be analysed with alpha at the 10 percent level.

It may also be interesting to compare growth from micron to millimetre size; with this in mind, we compare our results with those from mid-infrared spectroscopy using the Galactic sample of Gielen et al. (2011). However, these methods trace very different regions of the discs in terms of temperature and optical depth; mid-IR spectroscopy is sensitive to \sim micron-sized grains in the upper layers of the warm inner disc, while the FIR/sub-millimetre spectral index is sensitive to \sim millimetre-sized grains throughout the disc but particularly the cool mid-plane. Since these regions are not strongly connected, there is no reason to expect a meaningful correlation between these tracers.

Our sample has 31 sources in common with Gielen et al. (2011), of which 21 have robust measurements of α . For these sources, we compare α to the mass-fraction of small, medium, and large grains found by Gielen et al. (2011), by summing the fractions of each for each dust species, to leave the total mass-fraction of each grain size. Of these, the fraction of small grains can probably be considered the most robust, as a population of grains too large to

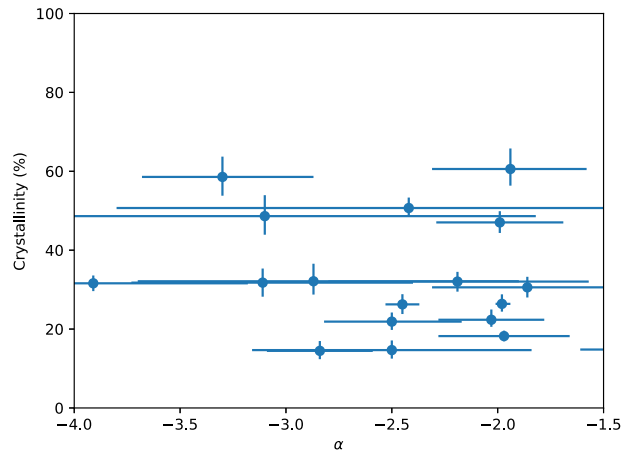


Figure 6. Scatter plot of the crystalline mass-fraction against α for the overlap between our sample and that of Gielen et al. (2011).

display features may be hiding in the continuum fit. These results are shown in Fig. 5. If grain growth to micron sizes is linked to growth to millimetre sizes, one would expect to see a correlation between α and the relative abundance of large grains seen in the mid-infrared, and an anticorrelation with the relative abundance of small grains.

It may also be interesting to consider the crystalline fraction, as an alternative proxy for dust evolution, and compare this with α . Once again, using the Gielen et al. (2011) sample, we sum the total mass fractions of crystalline Forsterite and Ortho-enstatite, plotting this against α in Fig. 6.

Unsurprisingly, given the weak connection between the regions of the disc that produce these observables, there is no evidence of any trends between grain size as probed by the mid-IR and by the far-IR. Similarly, the crystallinity does not correlate with the sub-millimetre spectral index. This is most likely a result of the disconnect between the regimes in question, as seen in PPDs (e.g. Ricci et al. 2010).

4.4 Comparison with other types of circumstellar discs

Having established that the presence of large dust grains is the most likely cause of the flat FIR/sub-millimetre spectra, it is interesting to compare this with other types of circumstellar discs. This may

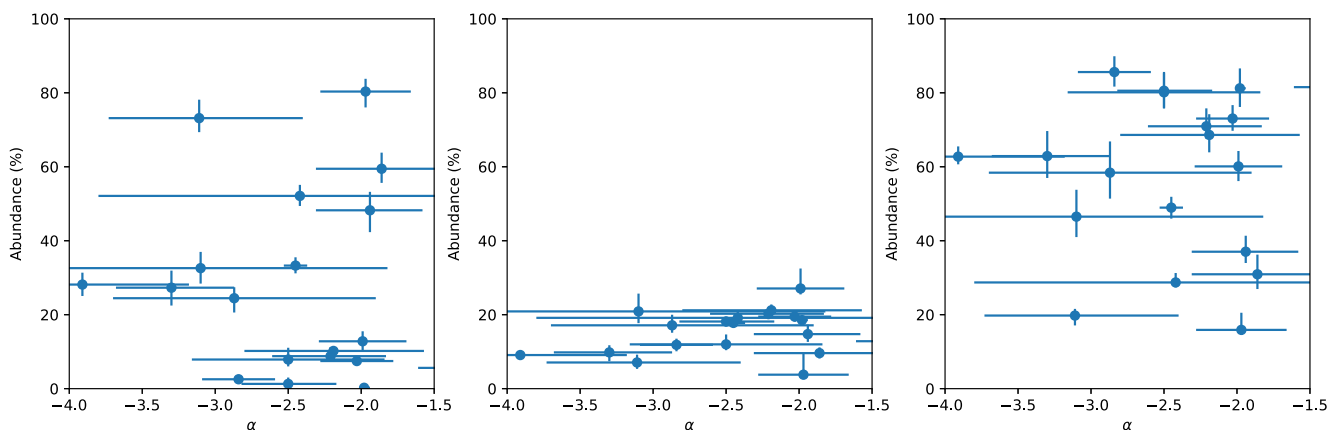


Figure 5. Scatter plots of the mass-fractions of small (left), medium (middle), and large (right) grains against α for the overlap between our sample and that of Gielen et al. (2011).

help to elucidate the formation mechanism of the large grains and hence the time-scales on which grain growth may be taking place.

The two most obvious comparison samples are the gas-rich, optically thick discs around young pre-main-sequence stars (PPDs), and the gas-poor, optically thin dust discs found around main sequence stars (DDs). In PPDs, the presence of gas damps the relative velocities of grains, and so collisions result in grain growth, while the lack of gas in DDs allows a collisional cascade to proceed unimpeded, resulting in the production of a large population of small grains. We select two samples: the Taurus PPD sample of Andrews & Williams (2005) and a sample of field DDs (MacGregor et al. 2016; Marshall et al. 2017). In order to make a distribution comparable to the histogram shown in Fig. 1, we sample from the distributions of published values assuming that they are normally distributed with (μ, σ) , respectively, equal to the published value and uncertainty of α . We draw samples from these distributions until the number of samples for each group of literature data matches the total number of MCMC samples used to construct the histogram shown in Fig. 1. The results of this sampling are shown in Fig. 7.

The peak of our sample lies intermediate to the two literature samples, but the cumulative distribution function is rather more similar to the PPD sample, with a longer tail of very low values of α . We quantify this by examining the sum of the differences between the two other distributions and the post-AGB distribution; this is about 30 per cent smaller for the PPD than the DD sample. This supports the expectation that these large grains are indeed formed *in situ* from material expelled and trapped in the circumstellar discs, rather than there being two populations of dust: newly formed small grains and larger grains produced by a population of parent bodies that somehow survived the post-MS evolution of the star. Furthermore, the sheer mass of dust would require an unfeasible amount of solid material to be present in the form of planetesimals at the end of the main sequence lifetime of these stars to produce the observed dust through a collisional cascade.

4.5 Post-AGB time-scales

The lifetimes of post-AGB stars are dictated by the time it takes for the photosphere to heat up sufficiently to begin ionizing the circumstellar envelope, creating a (pre-)PN. Single-star models predict that this time-scale is a strong function of initial stellar mass, and while it can be as short as decades at high masses, it is unlikely to be greater than 10^4 yr (Herwig 2005; Miller Bertolami 2016). However, as the accretion of material from the disc tends to inflate the star (leading to a cooler photosphere), this time-scale is not likely to be directly applicable in the case of the systems under consideration here and should be longer. Recent work by Oomen et al. (2019) that aims to explain the observed elemental depletions in post-AGBs through accretion shows that the increase in post-AGB lifetime is between a factor of 2 and 5, provided that the accretion rate is high enough (initially $>10^{-7} M_{\odot} \text{ yr}^{-1}$) and enough mass exists in the disc ($\sim 10^{-2} M_{\odot}$) to fuel long-term accretion. Assuming that this can be multiplied by the single-star evolutionary time-scale would give a range from 20 kyr to 50 kyr. Taking this at face value, and including an additional uncertainty of a factor of a few, we would infer that the lifetime of the post-AGB disc systems, which we expect to come from stars with relatively low initial masses, is typically a few times 10^4 up to perhaps a few times 10^5 yr.

A small selection of observational constraints also exists for objects in our sample. Bujarrabal et al. (2007), Bujarrabal et al. (2015), Bujarrabal et al. (2016), and Bujarrabal et al. (2017) have

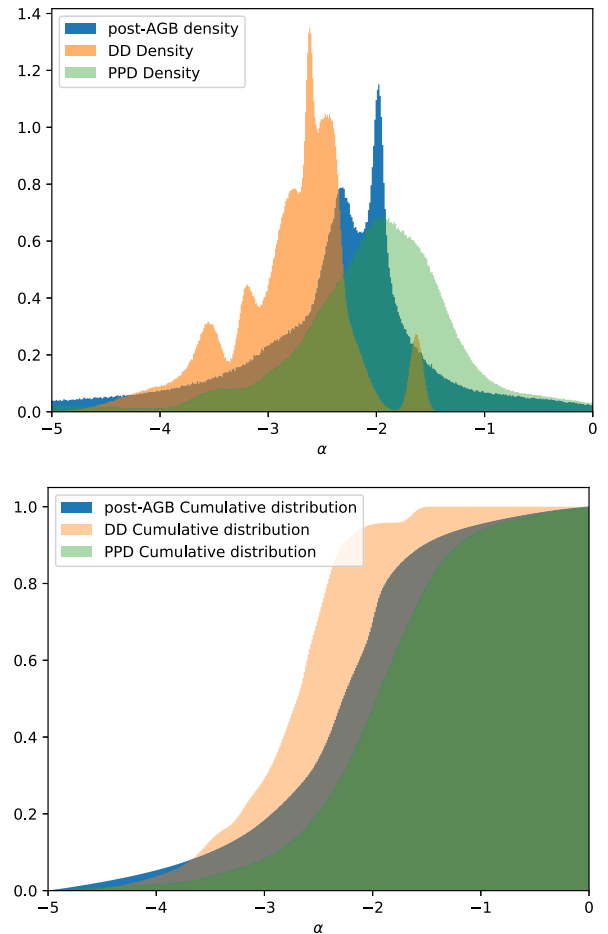


Figure 7. *Top:* Comparison of the histograms of the alpha values for our sample (blue) with those for a sample of protoplanetary discs in Taurus (Andrews & Williams 2005, green) and a sample of debris discs in the field (MacGregor et al. 2016; Marshall et al. 2017, yellow). The peak of the distribution for our sample is intermediate to the two samples but visually more similar to the protoplanetary disc sample. *Bottom:* As above, showing the cumulative distributions. It is clear that the distribution of α , and hence maximum grain size, is significantly different in debris discs when compared to the other two populations, lacking both very high and very low values of α .

resolved the discs of four objects in molecular lines (primarily ^{12}CO and ^{13}CO), revealing the Keplerian rotation of the discs and detecting or placing stringent limits on outflows. Using line radiative-transfer models, they find disc masses of $\sim 10^{-2} M_{\odot}$ and, based on the ratio of the disc mass to the outflow, disc lifetimes between 5000 and 20 000 yr, towards the lower end of that expected based on the work of Oomen et al. (2019).

However, the uncertainties on these observational time-scales are currently poorly known. The ^{12}CO lines are typically optically thick, significantly increasing the uncertainty on mass determinations, and while in most cases they have simultaneously fitted ^{13}CO , with only a single line this is still prone to uncertainty. In addition, the simplified modelling neglects a number of parameters that have been shown to play important roles in models of PPDs, such as the structure of the disc. For example, it has been shown that the amount of flaring in the disc can have a dramatic impact on the line fluxes (Woitke et al. 2010), and if this is not taken into account, it will have a large impact on the mass determined for the disc. Given

these limitations, the uncertainties on these models are difficult to quantify but may approach an order of magnitude, bringing them into better agreement with the results of Oomen et al. (2019).

4.6 Time-scales for grain growth

Our sample of post-AGB stars all have discs with large dust grains, but it is very unlikely that they all have the estimated maximum post-AGB age. Not all stars will reach that maximum lifetime, given a range of initial masses and binary/disc configurations. Furthermore, the sample likely covers a large range of post-AGB ages between zero and their maximum post-AGB lifetimes. The existence of a single population of grain sizes implies that either all members started from similar conditions or they evolve towards similarity on a time-scale much shorter than they are evolving.⁵

Thus, the grain growth time-scale is not constrained in our work by the maximum post-AGB lifetime; instead, it must be close to the post-AGB age of the youngest star in the sample, at least for that particular system. This is almost certainly much less than the maximum post-AGB lifetime. Therefore, if we accept the post-AGB lifetime of 10^5 yr discussed in the previous section as an upper limit, the grain growth time-scale must be $<<10^5$ yr and potentially as short as 10^3 yr.

More specifically, we infer that either dust grains had already grown to large sizes before the post-AGB phase began, or that the time-scale for grain growth to millimetre sizes is effectively instantaneous compared to the post-AGB lifetime, i.e. $t_{\text{mm}} < <t_{\text{pAGB}}$, so that all post-AGB discs rapidly converge to the same conditions, and hence it follows from the earlier discussion on lifetimes that $t_{\text{mm}} < <10^5$ yr, perhaps by orders of magnitude (i.e. 10^3 – 10^4 yr). The first of these scenarios implies that a significant population of dust became trapped in a long-lived disc while the star was still on the AGB, as the sizes of grains that form in evolved-star winds are typically ~ 0.05 – $0.5\mu\text{m}$ in size depending on the chemistry of the source (Höfner 2008; Norris et al. 2012; Scicluna et al. 2015; Nanni 2018); these sources are believed to be binaries, and hence this is not implausible. Recent observations have shown that some massive, highly evolved AGB stars do indeed host dense tori (Decin et al. 2019) but the high initial masses of these stars make them unlikely to be the progenitors of the post-AGB disc systems under consideration. The majority of a star’s mass loss occurs at the end of the AGB in a superwind, meaning that the majority of the material to be trapped should have become so only shortly before the star evolved off the AGB. If interactions with the companion are responsible for truncating the AGB phase (Van Winckel 2003) then the mass-loss episode could be even more constrained in time.

In the latter scenario, dust evolution is taking place in these systems on time-scales of thousands of years. This makes them an extreme laboratory for studying the physics of dust growth and processing. In comparison, PPDs are expected to have lifetimes of several megayears. Models of dust evolution in PPDs are divided: Birnstiel et al. (2010) do not predict the formation of $\gtrsim 100\text{-}\mu\text{m}$ particles on time-scales $\lesssim 10^5$ yr unless fragmentation is excluded, while Birnstiel, Klahr & Ercolano (2012) predict the efficient formation of millimetre- to centimetre-sized particles in the inner disc on time-scales of only 10^4 yr. However, given the difference in physical conditions between post-AGB and PPDs, it is not clear how easily this transfers from one to the other. New dust evolution models

tailored to post-AGB discs may help improve our understanding of grain growth by providing complementary constraints.

As the dust processing in molecular clouds and Class 0/Class 1 YSOs is poorly understood, the initial sizes of dust in PPDs is poorly known but may be larger than in AGB outflows. Nevertheless, the short grain growth time-scale suggested by post-AGB discs challenges models of grain growth in discs in a similar manner to recent observations of polarized (sub-)millimetre observations of YSOs, which are sometimes interpreted as a result of strong self-scattering and hence the presence of \sim millimetre-sized grains much earlier, in the Class 0/1 stage of pre-main-sequence evolution (e.g. Cox et al. 2015; Sadavoy et al. 2018). Similarly, radiative-transfer modelling has suggested the presence of millimetre- or even centimetre-sized grains in a sample of class I discs in Taurus (Sheehan & Eisner 2017). If these short time-scales are replicated in PPDs, it may explain the observational evidence of planet formation at the earlier Class 0/1 stages, as seen in, e.g. HL Tau (ALMA Partnership et al. 2015).

5 CONCLUSIONS

We present a consistent analysis of *Herschel*, SMA, and literature FIR/(sub-)millimetre fluxes of a sample of 46 post-AGB discs. By fitting power laws to the emission in this wavelength range, we find that the spectral indices α of these objects are concentrated in the range $-2.5 \leq \alpha \leq -2$, indicating that the grain-sized distribution in these discs extends to at least several hundred microns. The inclusion of long wavelength data is shown to be key to reducing the uncertainty in the determination of α for any given source, and hence surveys of these sources at wavelengths longer than $500\mu\text{m}$ should be considered a priority to understand whether the multiple sharp peaks seen in the distribution of spectral indices are real, or if there is a single population of spectral indices in post-AGBs.

We compare our results with mid-infrared measurements of grain growth for a subset of sources. Tracers of grain processing in the mid-IR (fraction of \sim micron-sized grains, crystalline fraction) do not correlate with α . This probably reflects the fact that the two tracers are sensitive to dust in very different regions of the discs.

The large dust mass of these discs and similarity of the distribution of spectral indices to those of PPDs indicate that this difference in spectral slope from interstellar dust is a result of *in situ* grain growth. Based on the expected sizes of newly formed dust grains around AGB stars, it is clear that a significant amount of grain growth has occurred; grain growth to sizes of at least several hundred microns is ubiquitous in post-AGB disc systems. The relatively short lifetimes of these discs, and the absence of any evolution of the observed α values with stellar effective temperature (a measure of age), show that all the discs must converge to the same state on a time-scale much shorter than their post-AGB evolutionary time-scale. Hence, grain growth to these sizes is a rapid process ($\tau_{\text{mm}} < <10^5$ yr), making them an extreme laboratory for studying dust growth, with important implications for dust in YSOs and PPDs.

Dust growth has been demonstrated up to millimetre sizes through mutual collisions, but the centimetre-sized barrier is insurmountable due to mutual velocities and low-surface adhesion resulting in bouncing rather than sticking between the largest grains (Blum 2010; Windmark et al. 2012b; Testi et al. 2014b). However, if larger grains are already present in the disc, further growth of small dust grains beyond the centimetre-sized barrier is a rapid process ($\sim 10^4$ yr; Windmark et al. 2012a). This barrier to growth can also be overcome by assuming some ‘stickier’ dust, which may

⁵This is particularly true, given that different sources will be evolving on different time-scales due to their different masses.

provide pathways towards the formation of a second generation of planetesimals.

To further understand these enigmatic objects and the insights they can provide on the physics of grain growth, several avenues should be explored. First, if the analogy with PPDs holds, we expect that different sized grains will exist in different regions of the disc. In this case, the integrated spectral index is not sufficient, and resolved sub-millimetre imaging of the discs is required to reveal the importance and time-scales of dust drift and settling. However, to understand whether post-AGB discs really are shorter lived analogues of PPDs, we must understand their origins. Kervella et al. (2015) recently detected an edge-on disc around the nearby AGB star L₂ Pup, although its relationship to post-AGB discs remains unclear. ALMA observations revealed a candidate sub-stellar object (Kervella et al. 2016) in the disc, which may be responsible for the recent and rapid formation of the disc. Continued monitoring of L₂ Pup, and other evolved systems with discs such as BP Psc (de Boer et al. 2017), will be key to understanding the formation of these discs and whether the physics is indeed similar to PPDs.

ACKNOWLEDGEMENTS

The authors are grateful to Hans Van Winckel for useful comments and discussion on the topic and to the anonymous referee whose feedback has helped improve this manuscript. In addition to the software explicitly cited above, this paper made use of Astropy (Astropy Collaboration 2013; Greenfield et al. 2013) and Astroquery (Ginsburg et al. 2016).

The Sub-Millimeter Array is a joint project between the *Smithsonian Astrophysical Observatory* and the Academia Sinica Institute of Astronomy and Astrophysics and is funded by the Smithsonian Institution and the Academia Sinica.

Herschel is an ESA space observatory with science instruments provided by European-led Principal Investigator consortia and with important participation from NASA.

This research has made use of the SIMBAD database, operated at CDS, Strasbourg, France (Wenger et al. 2000).

This research has made use of NASA's Astrophysics Data System.

This research has been supported by the Ministry of Science and Technology of Taiwan under grants MOST104-2628-M-001-004-MY3 and MOST107-2119-M-001-031-MY3, and by Academia Sinica under grant AS-IA-106-M03. This work benefited from the FEARLESS collaboration (FatE and AfteRLife of Evolved Solar Systems, PI: S. Ertel).

Scripts to reproduce this analysis are available at <http://github.com/psicicluna/GrainGrowthInPostAGBs>. They are also available on figshare along with the data at <https://figshare.com/account/home/projects/75495>.

REFERENCES

ALMA Partnership et al., 2015, *ApJ*, 808, L3
 Andrews S. M., Williams J. P., 2005, *ApJ*, 631, 1134
 Astropy Collaboration, 2013, *A&A*, 558, A33
 Balog Z. et al., 2014, *Exp. Astron.*, 37, 129
 Birnstiel T., Andrews S. M., 2014, *ApJ*, 780, 153
 Birnstiel T., Dullemond C. P., Brauer F., 2010, *A&A*, 513, A79
 Birnstiel T., Klahr H., Ercolano B., 2012, *A&A*, 539, A148
 Blum J., 2010, *Res. Astron. Astrophys.*, 10, 1199
 Boudet N., Mutschke H., Nayral C., Jäger C., Bernard J.-P., Henning T., Meny C., 2005, *ApJ*, 633, 272
 Bujarrabal V., Castro-Carrizo A., Alcolea J., Neri R., 2005, *A&A*, 441, 1031

Bujarrabal V., Van Winckel H., Neri R., Alcolea J., Castro-Carrizo A., Deroo P., 2007, *A&A*, 468, L45
 Bujarrabal V., Castro-Carrizo A., Alcolea J., Van Winckel H., Sánchez Contreras C., Santander-García M., Neri R., Lucas R., 2013, *A&A*, 557, L11
 Bujarrabal V., Castro-Carrizo A., Alcolea J., Van Winckel H., 2015, *A&A*, 575, L7
 Bujarrabal V., Castro-Carrizo A., Alcolea J., Santander-García M., Van Winckel H., Sánchez Contreras C., 2016, *A&A*, 593, A92
 Bujarrabal V., Castro-Carrizo A., Alcolea J., Van Winckel H., Sánchez Contreras C., Santander-García M., 2017, *A&A*, 597, L5
 Cohen M., Van Winckel H., Bond H. E., Gull T. R., 2004, *AJ*, 127, 2362
 Cox E. G. et al., 2015, *ApJ*, 814, L28
 de Boer J. et al., 2017, *MNRAS*, 466, L7
 de Ruyter S., Van Winckel H., Dominik C., Waters L. B. F. M., Dejonghe H., 2005, *A&A*, 435, 161
 de Ruyter S., Van Winckel H., Maas T., Lloyd Evans T., Waters L. B. F. M., Dejonghe H., 2006, *A&A*, 448, 641
 Decin L. et al., 2019, *Nature Astron.*, 3, 408
 Ertel S. et al., 2019, *AJ*, 157, 110
 Fedele D., van den Ancker M. E., Henning T., Jayawardhana R., Oliveira J. M., 2010, *A&A*, 510, A72
 Foreman-Mackey D., Hogg D. W., Lang D., Goodman J., 2013, *PASP*, 125, 306
 Garufi A. et al., 2017, *A&A*, 603, A21
 Gáspár A., Psaltis D., Rieke G. H., Özel F., 2012, *ApJ*, 754, 74
 Gezer I., Van Winckel H., Bozkurt Z., De Smedt K., Kamath D., Hillen M., Manick R., 2015, *MNRAS*, 453, 133
 Gielen C. et al., 2011, *A&A*, 533, A99
 Ginsburg A. et al., 2016, astroquery v0.3.1. <https://doi.org/10.5281/zenodo.44961>
 Gledhill T. M., Bains I., Yates J. A., 2002, *MNRAS*, 332, L55
 Greenfield P. et al., 2013, Astrophysics Source Code Library, record ascl:1304.002
 Griffin M. J. et al., 2010, *A&A*, 518, L3
 Herwig F., 2005, *ARA&A*, 43, 435
 Hillen M. et al., 2014, *A&A*, 568, A12
 Hillen M., de Vries B. L., Menu J., Van Winckel H., Min M., Mulders G. D., 2015, *A&A*, 578, A40
 Hirashita H., Voshchinnikov N. V., 2014, *MNRAS*, 437, 1636
 Höfner S., 2008, *A&A*, 491, L1
 Juhász A. et al., 2010, *ApJ*, 721, 431
 Kamath D., Wood P. R., Van Winckel H., 2014, *MNRAS*, 439, 2211
 Kamath D., Wood P. R., Van Winckel H., 2015, *MNRAS*, 454, 1468
 Kervella P. et al., 2015, *A&A*, 578, A77
 Kervella P., Homan W., Richards A. M. S., Decin L., McDonald I., Montargès M., Ohnaka K., 2016, *A&A*, 596, A92
 MacGregor M. A. et al., 2016, *ApJ*, 823, 79
 Marshall J. P., Maddison S. T., Thilliez E., Matthews B. C., Wilner D. J., Greaves J. S., Holland W. S., 2017, *MNRAS*, 468, 2719
 Matthews B. C., Krivov A. V., Wyatt M. C., Bryden G., Eiroa C., 2014, *Protostars and Planets VI*. University of Arizona Press, Tucson, AZ, p. 521
 Mennella V., Brucato J. R., Colangeli L., Palumbo P., Rotundi A., Bussoletti E., 1998, *ApJ*, 496, 1058
 Miller Bertolami M. M., 2016, *A&A*, 588, A25
 Miotello A., Testi L., Lodato G., Ricci L., Rosotti G., Brooks K., Maury A., Natta A., 2014, *A&A*, 567, A32
 Molinari S. et al., 2010, *A&A*, 518, L100
 Molinari S. et al., 2016, *A&A*, 591, A149
 Molster F. J. et al., 1999, *Nature*, 401, 563
 Nanni A., 2018, *MNRAS*, 482, 4726
 Norris B. R. M. et al., 2012, *Nature*, 484, 220
 Oomen G.-M., Van Winckel H., Pols O., Nelemans G., Escorza A., Manick R., Kamath D., Waelkens C., 2018, *A&A*, 620, A85
 Oomen G.-M., Van Winckel H., Pols O., Nelemans G., 2019, *A&A*, 629, A49
 Ossenkopf V., 1993, *A&A*, 280, 617

- Osterbart R., Langer N., Weigelt G., 1997, *A&A*, 325, 609
- Ott S., 2010, in Mizumoto Y., Morita K.-I., Ohishi M., eds, ASP Conf. Ser. Vol. 434, *Astronomical Data Analysis Software and Systems XIX*. Astron. Soc. Pac., San Francisco, p. 139
- Pilbratt G. L. et al., 2010, *A&A*, 518, L1
- Planck Collaboration XI, 2014, *A&A*, 571, A11
- Poglitsch A. et al., 2010, *A&A*, 518, L2
- Ricci L., Testi L., Natta A., Brooks K. J., 2010, *A&A*, 521, A66
- Roccatagliata V., Henning T., Wolf S., Rodmann J., Corder S., Carpenter J. M., Meyer M. R., Dowell D., 2009, *A&A*, 497, 409
- Sadavoy S. I. et al., 2018, *ApJ*, 859, 165
- Sahai R., Morris M., Sánchez Contreras C., Claussen M., 2007, *AJ*, 134, 2200
- Sahai R., Claussen M. J., Schnee S., Morris M. R., Sánchez Contreras C., 2011, *ApJ*, 739, L3
- Scicluna P., Siebenmorgen R., Wesson R., Blommaert J. A. D. L., Kasper M., Voshchinnikov N. V., Wolf S., 2015, *A&A*, 584, L10
- Sheehan P. D., Eisner J. A., 2017, *ApJ*, 851, 45
- Testi L. et al., 2014a, *Protostars and Planets VI*. University of Arizona Press, Tucson, AZ, p. 339
- Testi L. et al., 2014b, in Beuther H., Klessen R. S., Dullemond C. P., Henning T., eds, *Protostars and Planets VI*. University of Arizona Press, Tucson, p. 339
- Van Winckel H., 2003, *ARA&A*, 41, 391
- Van Winckel H., Lloyd Evans T., Reyniers M., Deroo P., Gielen C., 2006, *Mem. Soc. Astron. Italiana*, 77, 943
- Wells D. C., 1985, *Nrao'S Astronomical Image Processing System (AIPS)*. Springer US, Boston, MA, p. 195
- Wenger M. et al., 2000, *A&AS*, 143, 9
- Williams J. P., Cieza L. A., 2011, *ARA&A*, 49, 67
- Windmark F., Birnstiel T., Güttler C., Blum J., Dullemond C. P., Henning T., 2012a, *A&A*, 540, A73
- Windmark F., Birnstiel T., Ormel C. W., Dullemond C. P., 2012b, *A&A*, 544, L16
- Woitke P., Pinte C., Tilling I., Ménard F., Kamp I., Thi W. F., Duchêne G., Augereau J. C., 2010, *MNRAS*, 405, L26
- Wright E. L. et al., 2010, *AJ*, 140, 1868
- Wyatt M. C., Panić O., Kennedy G. M., Matrà L., 2015, *Ap&SS*, 357, 103
- Zeidler S., Mutschke H., Posch T., 2015, *ApJ*, 798, 125

This paper has been typeset from a $\text{\TeX}/\text{\LaTeX}$ file prepared by the author.